2023 IEEE International Conference on Robotics and Automation (ICRA 2023)
May 29 - June 2, 2023. London, UK

Heading Control of a Long-Endurance Insect-Scale Aerial Robot Powered by Soft Artificial Muscles

Yi-Hsuan Hsiao, Suhan Kim, Zhijian Ren, and YuFeng Chen*

***Abstract*— Aerial insects demonstrate fast and precise heading control when they perform body saccades and rapid escape maneuvers. While insect-scale micro-aerial-vehicles (IMAVs) have demonstrated early results on heading control, their flight endurance and heading angle tracking accuracy remain far inferior to that of natural fliers. In this work, we present a long endurance sub-gram aerial robot that can demonstrate effective heading control during hovering flight. Through using a tilted wing stroke-plane design, our robot demonstrates a 10-second flight where it tracks a desired yaw trajectory with maximum and root-mean-square (RMS) error of 14.2° and 5.8°. The new robot design requires 7% higher lift forces for enabling heading angle control, which creates higher stress on wing hinges and adversely influences robot endurance. To address this challenge, we developed novel 3-layered wing hinges that exhibit 1.82 times improvement of lifetime. With the new wing hinges, our robot demonstrates a 40-second hovering flight – the longest among existing sub-gram IMAVs. These results represent substantial improvement of flight capabilities in soft-actuated IMAVs, showing the potential of operating these insect-like fliers in cluttered natural environments.**

I. Introduction

Agile aerial insects can demonstrate exquisite flight maneuvers such as body saccades [1] and rapid recovery from disturbances [2]. Achieving these capabilities require visual feedback [3] and accurate control of the insect's heading angle during flight. Most two-winged insects (e.g., honey bees and flies) control heading angles through commanding asymmetric wing pitch motions using a specific set of flight muscles [2]. Inspired by these natural fliers, recently developed mesoscale (15 – 30 g) flapping-wing robots [4], [5] demonstrate heading control using a similar strategy.

Sub-gram micro-aerial-vehicles (MAVs) face unique fabrication and actuation challenges. Although these MAVs have demonstrated hovering and trajectory following capability [6], [7], it remains challenging to control the heading angle since the wing pitch motion of these robots cannot be actively regulated. This property of underactuation substantially limits insect-scale MAVs from performing insect-like tasks such as gaze stabilization and tracking of a desired target.

These authors are with the Research Laboratory of Electronics, Department of Electrical Engineering and Computer Science, Massachusetts Institute of Technology (MIT), Cambridge, MA, USA (e-mail:yhhsiao,suhank,zhijianr,yufengc@mit.edu).

*Corresponding author.

This work was partially supported by the National Science Foundation (FRR-2202477), and the Research Laboratory of Electronics, MIT (2244181). Any opinions, findings, and conclusions or recommendations expressed in this material are those of the authors and do not necessarily reflect the views of the National Science Foundation. Yi-Hsuan Hsiao is partially supported by the Taiwanese Graduate Fellowship. Suhan Kim and Zhijian Ren are supported by the Mathworks Engineering Fellowship.

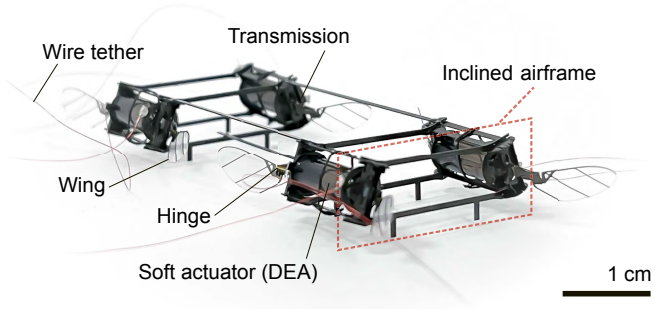

Fig. 1. An image of a 680 mg micro-aerial-robot driven by dielectric elastomer actuators. The robot has 4 modules that are assembled into an inclined airframe. Each module has an airframe, a dielectric elastomer actuator (DEA), two linear four-bar transmissions, wing hinges, and wings. The robot requires external power supply through its tethers.

To address this challenge, recent studies [8]–[11] developed a new control strategy for generating flight torques and controlling the heading angle. The researchers proposed a split-cycle [9], [11] design in which the wing upstroke and downstroke motions become asymmetric. This asymmetric wing stroke motion induces differential drag forces, which lead to asymmetric wing pitch motion and a net control torque. Under this design, Chukewad et al. demonstrated tracking of heading angle in short hovering flights (∼2 seconds) [9]. McGill et al. implemented a similar design and demonstrated longer flights (∼6 seconds) with improved accuracy [11]. While this split-cycle design enables heading angle control during hovering flights, it suffers two major shortcomings. First, it requires higher harmonic control signals to generate asymmetric wing stroke motions, which cause a reduction of cycle-averaged lift [11]. Second, the control torque is small (∼0.05 mN·mm) compared to the robot's moment of inertia (∼0.45 g·mm^2). Consequently, in these flight demonstrations, the robot is tied to a safety tether and it flies in close proximity of the resting point to minimize external torque disturbances.

In recent years, our team has developed SoftFly, a soft-actuated sub-gram MAV [12]–[15] that is driven by Dielectric Elastomer Actuators (DEAs). Owing to actuator robustness, our robot has demonstrated unique maneuvers such as in-flight collision recovery and somersault [13]. However, our robot has not demonstrated heading angle control due to challenges in nonlinear DEA actuation [12]. The existing actuation strategy leverages system resonance to attenuate higher harmonic modes. Consequently, our robot cannot achieve asymmetric wing stroke motions using a split-cycle approach [11]. This limitation requires a new design for enabling heading angle control.

In this work, we developed a new robot configuration for enabling heading angle control and designed new wing hinges for substantially improving flight endurance. Our robot weighs 680 mg, and it consists of 4 modules that are installed in an inclined airframe (Figure 1). The tilted stroke-plane design for sub-gram aerial robot is first proposed by Yang et al [16], but the robot could not demonstrate in-flight heading angle control due to a limited lift force. Our robot has a high lift-to-weight ratio (>3:1) [14] and it can generate additional lift forces as required by the new design. With a new flight controller, our robot demonstrated three 12-second hovering flights where it maintained a constant heading direction. The maximum and RMS heading angle errors are 8.9° and 5.6°, respectively. In addition, the robot can track a desired heading angle trajectory with a maximum and RMS error of 14.2° and 5.8°. In these flight demonstrations, each robot module needs to produce approximately 7% additional lift forces compared to previous robot designs [13], [14]. This requirement worsens wing hinge fatigue and reduces lifetime. Here, we developed a 3-layered wing hinge that showed a 1.82 times increase of endurance. Our robot demonstrated a 40-second hovering flight, which is over 2 times longer than that of existing sub-gram MAVs [14]. Our flight results demonstrate that soft-actuated IMAVs can achieve accurate heading angle control without sacrificing flight endurance. More importantly, the flight endurance exceed that of rigid-driven sub-gram MAVs [9]–[11], showing the unique promise of agile, robust, and controllable soft aerial robots.

II. Robot Design and Characterization

A. Tilted stroke-plane design for controlling heading angle

We designed a new robot configuration (Figure 2) for enabling heading angle control. The robot consists of 4 identical modules weighing 155 mg. Similar to that of our prior works [13], [14], each robot module has 2 wings and operates at 400 Hz. It generates a time-averaged lift force and no net drag force. A key difference between flapping-wing and rotary propulsion is that the flapping-wing module cannot produce a net torque with respect to the lift axis. If the four robot modules are assembled into a quadrotor-like configuration [13], [14], the robot cannot generate control torques along the body z-axis.

We propose a tilted stroke-plane design where each module is tilted by 20° (θ_t) with respect to the robot's body z-axis (Figure 2a). Figure 2a illustrates the robot coordinates and the roll (x-axis), pitch (y-axis), and yaw (z-axis) definitions. The lift force components that are parallel to the body z-axis control the robot pitch and roll motions through a similar design in a prior work [12]. The lift force components that are orthogonal to the body z-axis control the robot's rotation relative to the body z-axis, which is defined as the yaw angle θ. In Figure 2a, we illustrate the lift vectors of opposing pairs using different colors. When the red-colored pair generates a larger net lift compared to the blue-colored pair, the robot produces to a positive yaw torque without generating net

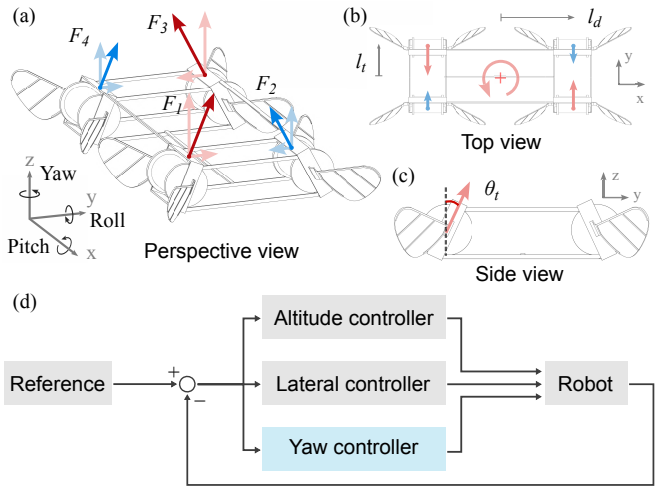

Fig. 2. Tilted stroke plane design and controller architecture. (a-c) Perspective (a), top (b), and side (c) view illustrations of the robot assembly. By increasing the lift forces of opposing module pairs (red), the robot can generate a control torque with respect to its body z-axis. This design allows the robot to control its heading angle during hovering flight. (d) An illustration of the controller design. We design a yaw controller (blue) in parallel with existing altitude and lateral controllers.

lateral forces. Figure 2b-c show the top and side views of this tilted stroke plane design.

Next, we construct a new flight controller for this robot. This controller design is based on our prior work [12] that developed a geometric controller for robot positions and roll and pitch rotations. Given a desired trajectory, the previous controller calculates the corresponding lift force (F) and torques (τ_x, τ_y). For this new robot, we can further generate yaw torque τ_z. The robot attitude dynamics is described by the Euler's equation:

$$\boldsymbol{I}\dot{\boldsymbol{\omega}} + \boldsymbol{\omega} \times \boldsymbol{I}\boldsymbol{\omega} = \boldsymbol{\tau}, \tag{1}$$

where $\boldsymbol{I}$ is the moment of inertia tensor, $\boldsymbol{\omega}$ is the angular velocity vector, and $\boldsymbol{\tau}$ is the net torque. We assume the cross term $\boldsymbol{\omega} \times \boldsymbol{I}\boldsymbol{\omega}$ is negligible. In addition, the roll and pitch angles are close to 0° during hovering flight, which leads to simplified rotational dynamics relative to the robot's body z-axis:

$$I_{zz}\ddot{\theta} = \tau_z - k_s\theta. \tag{2}$$

Here, the term $k_s\theta$ represents the torque contributed by the power tethers that act as a torsional spring. We implement a proportional-derivative (PD) controller for the robot's yaw rotation, which takes the form of:

$$\tau_z = k_s\theta + I_{zz}\ddot{\theta}_d + k_p(\theta_d - \theta) + k_d(\dot{\theta}_d - \dot{\theta}). \tag{3}$$

Here k_p and k_d are the proportional and derivative gains, θ_d, $\dot{\theta}_d$, and $\ddot{\theta}_d$ are the desired yaw motion, and θ, $\dot{\theta}$, and $\ddot{\theta}$ are the measured yaw motion. The closed-loop yaw dynamics is obtained by substituting equation 3 into equation 2:

$$0 = I_z(\ddot{\theta}_d - \ddot{\theta}) - k_p(\theta - \theta_d) - k_d(\dot{\theta}_d - \dot{\theta}). \tag{4}$$

We choose the parameters k_p and k_d to satisfy the Routh-Hurwitz stability condition. Along with the geometric attitude and altitude controllers [12], the combined controller calculates the desired lift force (F) and torques (τ_x, τ_y, τ_z). Based on the robot geometry, the desired lift force from each

robot module is calculated as:

$$\begin{bmatrix} F_1 \\ F_2 \\ F_3 \\ F_4 \end{bmatrix} = \begin{bmatrix} c\theta_t & c\theta_t & c\theta_t & c\theta_t \\ -l_t c\theta_t & l_t c\theta_t & l_t c\theta_t & -l_t c\theta_t \\ -l_d c\theta_t & -l_d c\theta_t & l_d c\theta_t & l_d c\theta_t \\ l_d s\theta_t & -l_d s\theta_t & l_d s\theta_t & -l_d s\theta_t \end{bmatrix}^{-1} \begin{bmatrix} F \\ \tau_x \\ \tau_y \\ \tau_z \end{bmatrix}, \quad (5)$$

where $c\theta_t$ and $s\theta_t$ are abbreviations for $\cos\theta_t$ and $\sin\theta_t$, and l_t and l_d are robot configuration dimensions as defined in Figure 2 ($l_t = 12$ mm and $l_d = 22$ mm). Compared to our prior works [12]–[14], this new design enables the control of the robot's yaw motion. However, to maintain robot hovering flight, each tilted module needs to generate a 7% higher lift force (Figure 2c), which further requires a 3% higher driving voltage and consumes 6% more electrical power. In this work, the robot is driven by offboard high voltage amplifiers (Trek 2220) that can easily supply the extra voltage and power. In addition to higher power consumption, the increase of required lift force leads to a larger wing stroke motion, which worsens wing hinge fatigue. In the next section, we introduce a new wing hinge design that mitigates fatigue and improves hinge lifetime.

B. 3-layered wing hinge design for improving flight endurance

We developed a new wing hinge that substantially improves endurance while operating at similar lift force conditions. Each robot module has 1 DEA and 2 wings. When a sinusoidal voltage waveform drives the DEA, the actuator elongates and contracts with a peak-to-peak displacement of 1.2 mm. This translational motion is converted into the robot's wing stroke rotation through a linear four-bar transmission. This wing stroke motion (Figure 3a and Supplementary Video part 1) is directly controlled by the DEA. While the wing moves along the stroke plane, it passively rotates along its leading-edge axis (Figure 3a and Supplementary Video part 1) due to competing aerodynamic and inertial effects. This underactuated pitching motion generates lift forces without requiring additional actuators. Prior studies [17]–[19] investigated the aerodynamic efficiency of flapping-wing propulsion under different wing stroke and pitch kinematics.

To achieve desirable passive pitching dynamics, it is critical to optimize the wing hinge stiffness. Prior studies [20], [21] used polyimide as a compliant flexure to mimic a torsional spring. They optimized the flexure design for RoboBee — an 80 mg flapping-wing robot driven by piezoelectric actuators — and achieved an impressive lifetime of 0.2 million cycles (approximately 2000 seconds). However, our robot weighs 2 times heavier and operates at 4 times higher frequency. Consequently, each wing hinge supports 2 times the aerodynamic loading and suffers a substantial reduction of lifetime due to faster wingbeat. In prior works, we found our hinge lifetime to be approximately 0.02 million cycles (40 seconds) when the robot operates at hovering conditions.

In this work, we found the tilted design further reduces hinge lifetime due to the need of higher lift force. Figure 3b shows a wing-hinge pair where the lower hinge is completely torn off. The inset in Figure 3b highlights the torn polyimide flexure. During the flapping-wing motion, a minor tear develops around the upper left polyimide corner. This crack gradually propagates towards the lower right corner until the wing hinge is torn apart. The red circles in Figure 3b highlight the tear locations.

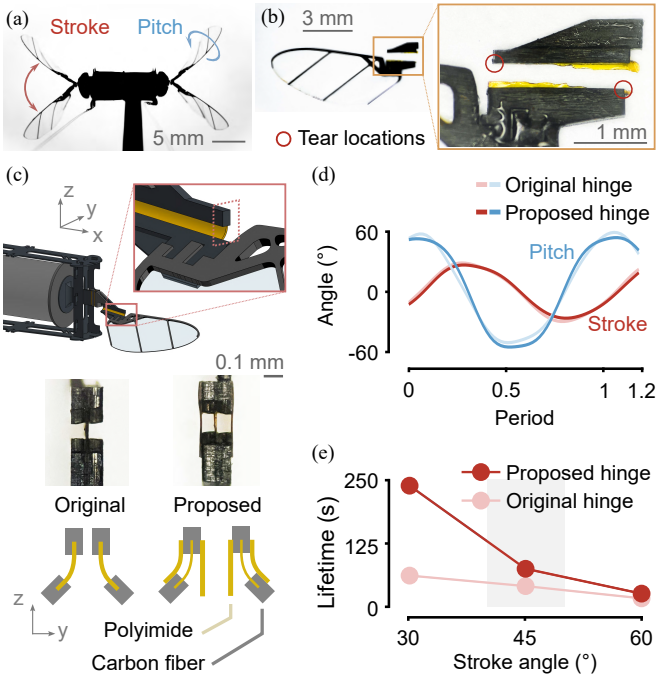

Fig. 3. Design and characterization of long endurance wing hinges. (a) A composite image of the robot's flapping-wing kinematics. The wing stroke and pitch motions are labelled in red and blue colors, respectively. (b) An image of a torn wing hinge. The inset highlights the tear locations along the polyimide flexure. (c) CAD model, side view images, and illustrations of the wing hinge. The CAD model shows a wing hinge that connects to the robot transmission and wing. The side view images compare the 1-layered and 3-layered hinges. The original hinge (left) consists of a single layer of polyimide flexure. The new hinge (right) consists of 3 layers of polyimide flexures. The outer layers are connected to the upper hinge part. (d) The robot exhibits similar stroke and pitch kinematics with these two types of wing hinges. (e) The 3-layered wing hinge exhibits longer lifetime than the original wing hinge when the robot operates at similar kinematic conditions (30°, 45°, and 60°).

One method of improving the hinge lifetime is to reduce the hinge bending curvature through rescaling hinge geometry [21]. However, this design requires a simultaneous increase of hinge width and length, which would substantially change the hinge inertia and the wing placement position. These changes would influence the robot resonance frequency and substantially impact lift force generation.

We propose a 3-layered hinge design that does not require rescaling the hinge geometry. In the original hinge design (Figure 3c), a single polyimide layer acts both as a torsional spring and a mechanical connection between the upper and lower hinge. When the hinge experiences fatigue, the hinge stiffness decreases and the wing pitch motion grows due to the aerodynamic loading. This increase of wing pitch amplitude represents an increase of hinge bending curvature, which worsens fatigue and accelerates hinge failure. Alternatively, we propose a 3-layered design (Figure 3c)

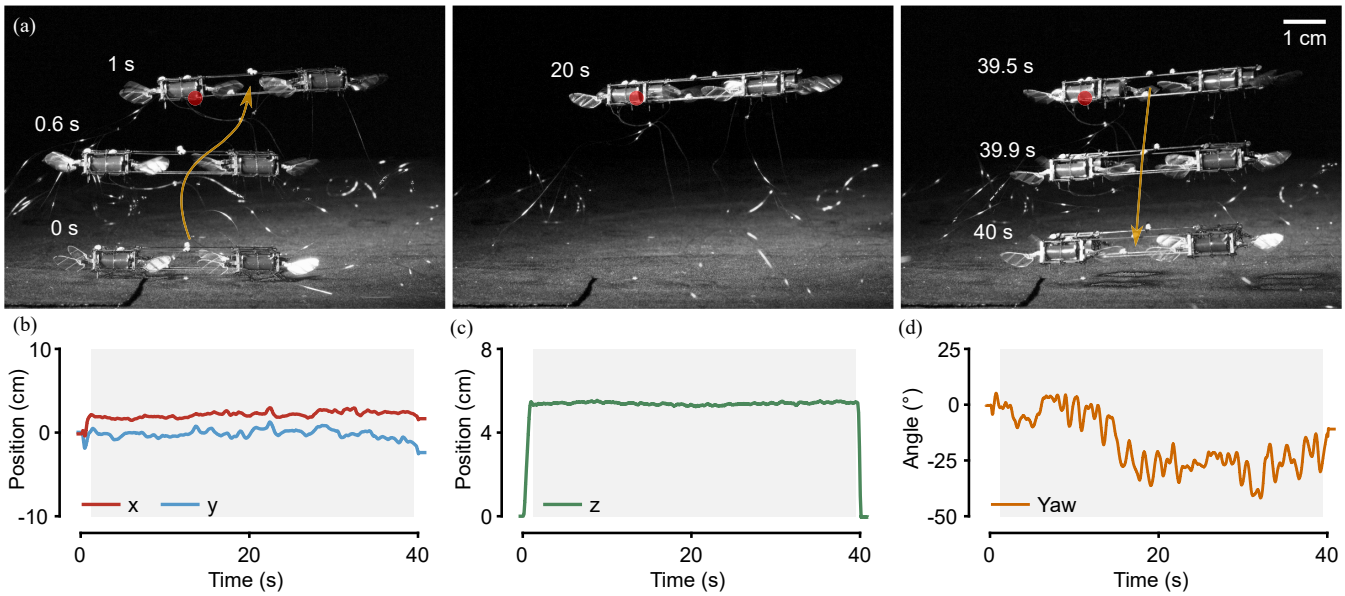

Fig. 4. A 40-second hovering flight without yaw control. (a) A sequence of composite images that show the robot hovers for 40 seconds at 5 cm above ground. The red dots indicate the location of the position setpoint. (b-c) Tracked robot lateral (b) and altitude (c) data during the flight. The RMS error of x, y, and z positions are 21.8 mm, 4.8 mm, and 3.0 mm, respectively. (d) Tracked yaw rotation as a function of time. Without turning on yaw control, the maximum heading angle error is 41.8°. The shaded regions exclude robot takeoff and landing.

that uncouples the spring component and the mechanical connection. The central layer is made of a thin polyimide sheet whose stiffness is around 10% of the outer layers. This central layer connects the upper and lower hinge parts. The outer two layers are made of a thicker polyimide sheet and they are only connected to the upper wing hinge. During the flapping-wing motion, each of the outer layers only provides restoring torques during half of the flapping cycle (Figure 3c). This design is advantageous because the softening of the central layer does not reduce the overall hinge stiffness. The outer layers do not experience bidirectional bending, and this mitigates hinge fatigue.

To validate this design, we fabricated 1-layered and 3-layered wing hinges and compared their performance. The width, length, and thickness of the 1-layered wing hinge are 2.15 mm, 0.09 mm, and 12.7 μm, respectively. The width and length of the 3-layered wing hinge are 2.15 mm and 0.11 mm. The thickness of the central and outer layers are 7.5 μm and 12.7 μm. According to equation (1) from Malka et al. [21], the stiffness of the 1-layered and 3-layered hinges are calculated to be 1.02×10^{-5} N·m·rad^{-1} and 1.01×10^{-5} N·m·rad^{-1}, respectively. We assembled these wing hinges into a robot module and conducted flapping-wing experiments. Figure 3d shows the tracked wing stroke and pitch kinematics. These experiments confirm the new hinge design can generate similar flapping-wing motion, which implies the robot produces similar lift and drag forces.

Next, we conducted a sequence of hinge endurance tests (Figure 3e) and observed the 3-layered hinge exhibits substantially improved lifetime. We designed three test cases where the wing stroke amplitude was set to 30°, 45°, and 60°, respectively. These wing stroke motions correspond to an approximate lift-to-weight ratio of 0.7, 1.0, and 1.7, respectively. To measure the hinge lifetime, we drove the robot at these conditions until observing hinge failure. As shown in Figure 3e, the 3-layered hinge shows higher endurance in all of the testing conditions. The shaded region indicates the robot hovering condition. We found the hinge lifetime increases from 40 seconds to 75 seconds. This substantial lifetime improvement enables long endurance flights and yaw-controlled flights in the following sections.

III. Flight Experiments

A. Experimental setup

We implemented the proposed flight controller in MATLAB Simulink and compiled it on a designated computer (Baseline Target Machine, Speedgoat). The controller runs at 10 kHz in the Simulink Real-Time environment, and the controlled signals are sent to the voltage amplifiers (677B, Trek) before being executed on the robot. The position and orientation of the robot are tracked by a motion capturing system (6 Vantage V5 cameras, Vicon), which has a tracking volume of 80 × 60 × 70 cm. In addition, the robot flapping-wing and flight videos are recorded by a high-speed camera (VEO V710, Phantom) for post-analysis.

B. Long-endurance hovering flight without yaw control

We performed a sequence of flight experiments with this newly-designed robot. First, we conducted a 40-second flight to demonstrate robot endurance. In this experiment, we switched off the yaw controller (Figure 2d) so the robot does not actively control its heading angle. Figure 4a shows composite images of this hovering flight, which is also shown in Supplementary Video part 2. This flight consists of a 1.0-second takeoff phase, a 38.5-second hovering phase, and a 0.5-second landing phase. In the hovering phase, the maximum and RMS lateral position errors are 32.2 mm and 22.1 mm, respectively (Figure 4b). The robot is commanded to hover 5 cm above ground, and the maximum and RMS altitude errors are 4.5 mm and 3.0 mm, respectively. Since

the robot's heading angle is not closed-looped controlled, we observed a slow drifting of the yaw angle (Figure 4c). Despite fine open-loop tuning on net yaw torque prior to this hovering flight, the maximum yaw error still reaches 41.8°.

This hovering flight represents the longest flight performed by sub-gram aerial robots. The integration of long-endurance soft actuators [14] and the enhanced wing hinges introduced in Sec. II-B enables the robot to withstand added mechanical stress caused by the tilted stroke-plane configuration. Furthermore, in this 40-second flight, the robot maintains small position and altitude errors that are comparable to shorter flights performed by other state-of-the-art sub-gram MAVs [6]. Based on the hinge endurance measurements in Sec. II-B, the robot's total flight time prior to hinge replacement is estimated to be 75 seconds. Before conducting this long endurance flight, we performed a sequence of short flights for tuning the controller parameters. These tuning flights consist of 15-20 seconds of operation. After performing the 40-second flight, we replaced all eight wing hinges to prepare for new flights under yaw control. Aside from the wing hinges, other robot components have substantially longer lifetime (>1000 seconds) and they do not require frequent replacement.

In this 40-second flight, we observed a noticeable drift of the robot's yaw angle. This may be caused by the ambient air flow, torques induced by the wire tether, and the unregulated force components perpendicular to the body z-axis. This undesired yaw motion motivates the need of controlling the robot's heading angle during flight; thus, in the following sections, we switched on the yaw controller to demonstrate heading angle control.

C. Hovering flight with a constant yaw setpoint

Followed by the 40-second hovering flight, we switched on the yaw controller and commanded the robot to hover around a constant setpoint. Figure 5a and Supplementary Video part 3 show a 12-second hovering flight where the desired yaw angle was 0°. The flight consists of 1-second ascent, 10-second hovering, and 1-second descent. The controller parameters, k_p and k_d (in Eq. 3), are set to 2.8×10^{-5} and 8.8×10^{-6}, respectively. The robot hovers 10 cm above ground. The upper panel in Figure 5b shows the tracked lateral position data, and the maximum and RMS error are 38.1 mm and 30.8 mm, respectively. The tracked altitude data (lower panel in Figure 5b) shows a maximum and RMS error of 8.2 mm and 6.0 mm, respectively. Furthermore, the maximum and RMS error of the yaw angle are 8.9° and 5.6°, respectively (Figure 5c). In contrast to performing a single long-endurance yaw-controlled flight demonstration, we conducted three 12-second hovering flights to show repeatability. In these three yaw-controlled flights, the yaw angle setpoint is 0°. The tracked lateral position, altitude, and yaw angle data of the other two flights are shown in Figure 5b-c with lighter colors. Compared to the 40-second hovering flight, the maximum and RMS yaw angle error are reduced by 78.7% and 74.4%, respectively.

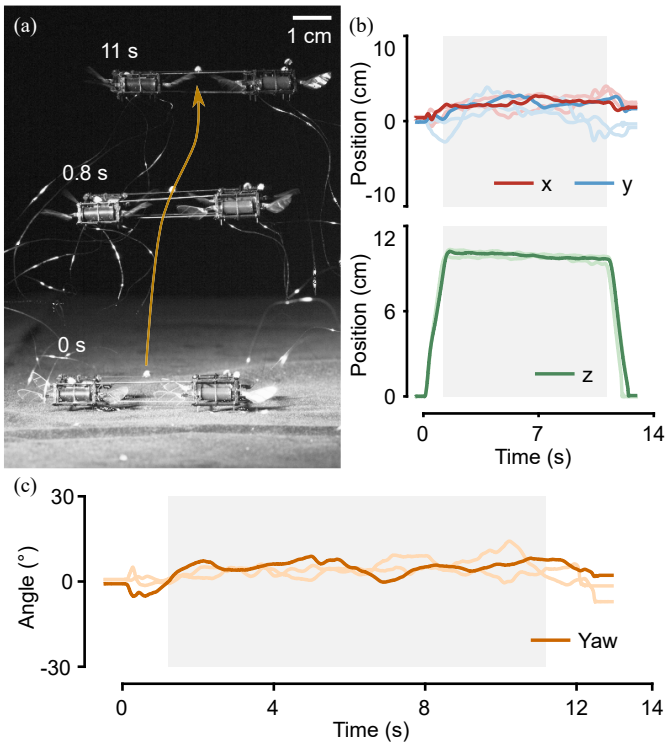

Fig. 5. 12-second hovering flights with yaw control. (a) A composite image that shows a 12-second hovering flight. The desired yaw angle is set to 0°. (b) Tracked lateral position (upper panel) and altitude (lower panel) of three 12-second flights. (c) Tracked yaw rotation of the same flights in (b). In (b-c), the darker colored curves correspond to the flight shown in (a). The shaded regions exclude robot takeoff and landing.

D. Hovering flight with yaw tracking

Next, we performed a 10-second hovering flight in which the robot tracks a desired yaw trajectory (Figure 6a and Supplementary Video part 4). The flight consists of 1-second ascent, 8.5-second hovering, and 0.5-second descent, and the controller parameters, k_s, k_p, and k_d (in Eq. 3), are set to 2.5×10^{-5}, 6.0×10^{-5}, and 9.2×10^{-6}, respectively. The desired and tracked yaw angles are shown in Figure 6b, where the positive and negative yaw setpoints are 30° and -60°, respectively. This result demonstrates the robot yaw motion can be controlled in both directions, and the robot can track a pre-determined time-varying reference trajectory with a maximum and RMS error of 14.2° and 5.8°, respectively. At the same time, the maximum and RMS lateral position errors are 30.4 mm and 18.4 mm (Figure 6c), and the maximum and RMS altitude error are 17.0 mm and 10.1 mm. While the position and altitude errors remain small (<35 mm), we found that positions and yaw motion are coupled due to assembly imperfections. When the robot turns in the positive direction with respect to the body z-axis, the robot drifts slightly in the positive y and z directions. In contrast, when the robot turns in the negative direction, it drifts in the negative y and z directions. This small error could be mitigated by implementing an integral term in the flight controller. The controller parameter values for the flights reported in Sec. III are documented in Table I.

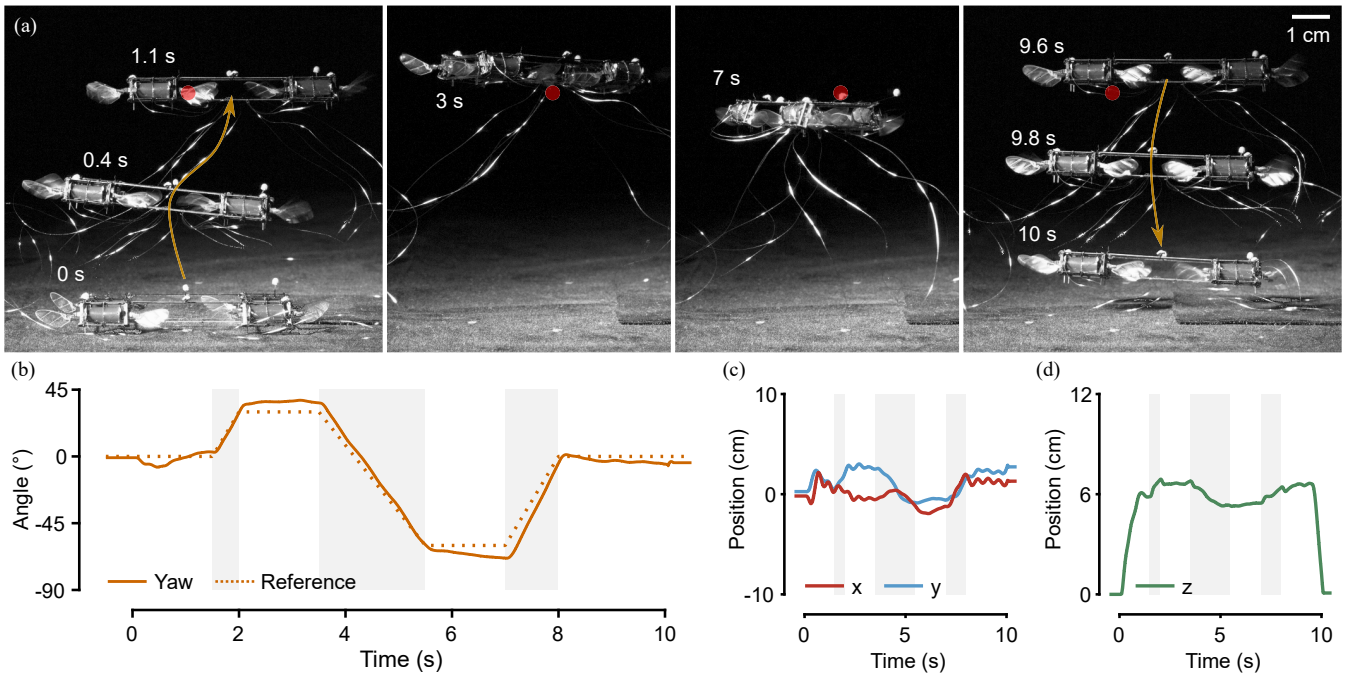

Fig. 6. A 10-second hovering flight that tracks a desired yaw trajectory. (a) A sequence of composite images that illustrate the 10-second flight. At t = 3 s and t = 7 s, the desired yaw angles are 30° and -60°, respectively. The red dots indicate the location of the position setpoint. (b) Desired (dotted) and measured (solid) yaw motion as a function of time. (c-d) Tracked lateral positions (c) and altitude (d). The shaded regions indicate the time where desired the yaw trajectory changes linearly.

TABLE I
Controller parameters of the reported flights.

Flight	λ_0	λ_1	λ_2	λ_3	Λ_0	Λ_1
Endurance (Fig. 4)	7756	4177	423	32	135	19
Yaw setpoint (Fig. 5)	8845	4310	467	32	90	18
Yaw tracking (Fig. 6)	9051	4442	335	32	90	18

*λ_i and Λ_i are parameters for attitude and altitude controllers as defined in Chen et al. [12], Supplementary Note S4.

TABLE II
Comparison of flight endurance and heading-angle tracking among sub-gram MAVs.

Robot	Flight time		RMS errors		Safety tether
	Yaw control		Lateral	Yaw	
	No	Yes	(mm)	Angle	
RoboBee [11] [22]	11 s	6 s	19.1⋆	4.1°⋆	Yes
RoboFly [9] [23]	5 s	2 s	13.6‡	18.9°	Yes
QAB [24]	N/A	9.5 s	33.5⊥	38°	Yes
SoftFly (this work)	40 s	10 s	18.4△	5.8°△	No

⋆The authors provided mean errors (not RMS) in [11].
‡Flight results without yaw-angle tracking from [23]. No lateral position errors found in [9].
⊥Calculated through the graphs reported by the authors.
△Based on yaw tracking flight in this work (Fig. 6).

IV. Discussion and Conclusion

In this work, we developed a 680 mg aerial robot based on the tilted stroke-plane design. Equipped with novel 3-layered wing hinges, the robot demonstrated a 40-second long-endurance hovering flight, three 12-second flights with a fixed yaw setpoint, and a 10-second flight with yaw trajectory tracking. Table II compares the flight performance of existing sub-gram MAVs that are capable of demonstrating in-flight yaw angle tracking. In comparison, our robot exhibits substantially longer flight endurance with similar accuracy. In addition, all other rigid-driven robots in Table II require a safety tether when performing yaw-controlled flights, while our soft-actuated SoftFly does not need one because of actuator robustness and structural resilience.

Furthermore, this work demonstrates that the tilted stroke-plane design is effective for enabling yaw control. This design outperforms the split-cycle methods [9], [11] in DEA-driven aerial robots since the higher harmonic control signals would be distorted and damped by the soft actuators that operate near resonance frequency. Another advantage of this design is that yaw torque generation only requires purely sinusoidal driving inputs, which can simplify future designs of onboard power electronics. In addition, this configuration enables simultaneous control of roll, pitch, yaw, and thrust commands, which is analogous to that of larger-scale tilted quadrotors [25]. Future works can leverage well-established control strategies from the quadrotor community to execute more challenging maneuvers in sub-gram MAVs. Furthermore, the new 3-layered wing hinges show a 1.82 times increase of lifetime without changing hinge inertia or stiffness. Both the tilted configuration and 3-layered hinges may benefit the IMAV research community, and they can be applied in rigid-driven MAVs.

More importantly, this work expands the flight capability of soft-actuated aerial robots. Combined with prior works [12]–[15], our robot has demonstrated tasks such as hovering flight [12], [14], in-flight collision recovery [13], somersault [13], electroluminescence-assisted motion tracking [15], 40-second long-endurance flight (this work), and yaw trajectory tracking (this work). Many of these flight capabilities are comparable to or even absent in the state-of-the-art rigid-driven sub-gram MAVs. These works demonstrate the unique potential of developing agile, robust, and multifunctional soft robots.

REFERENCES

[1] S. N. Fry, R. Sayaman, and M. H. Dickinson, "The aerodynamics of free-flight maneuvers in drosophila," *Science*, vol. 300, no. 5618, pp. 495–498, 2003.

[2] L. Ristroph, A. J. Bergou, G. Ristroph, K. Coumes, G. J. Berman, J. Guckenheimer, Z. J. Wang, and I. Cohen, "Discovering the flight autostabilizer of fruit flies by inducing aerial stumbles," *Proceedings of the National Academy of Sciences*, vol. 107, no. 11, pp. 4820–4824, 2010.

[3] D. L. Altshuler and M. V. Srinivasan, "Comparison of visually guided flight in insects and birds," *Frontiers in neuroscience*, vol. 12, p. 157, 2018.

[4] M. Karásek, F. T. Muijres, C. De Wagter, B. D. Remes, and G. C. De Croon, "A tailless aerial robotic flapper reveals that flies use torque coupling in rapid banked turns," *Science*, vol. 361, no. 6407, pp. 1089–1094, 2018.

[5] Z. Tu, F. Fei, L. Liu, Y. Zhou, and X. Deng, "Flying with damaged wings: The effect on flight capacity and bio-inspired coping strategies of a flapping wing robot," *IEEE Robotics and Automation Letters*, vol. 6, no. 2, pp. 2114–2121, 2021.

[6] K. Y. Ma, P. Chirarattananon, S. B. Fuller, and R. J. Wood, "Controlled flight of a biologically inspired, insect-scale robot," *Science*, vol. 340, no. 6132, pp. 603–607, 2013.

[7] Y. M. Chukewad, J. James, A. Singh, and S. Fuller, "Robofly: An insect-sized robot with simplified fabrication that is capable of flight, ground, and water surface locomotion," *IEEE Transactions on Robotics*, vol. 37, no. 6, pp. 2025–2040, 2021.

[8] S. B. Fuller, J. P. Whitney, and R. J. Wood, "Rotating the heading angle of underactuated flapping-wing flyers by wriggle-steering," in *2015 IEEE/RSJ International Conference on Intelligent Robots and Systems (IROS)*. IEEE, 2015, pp. 1292–1299.

[9] Y. M. Chukewad and S. Fuller, "Yaw control of a hovering flapping-wing aerial vehicle with a passive wing hinge," *IEEE Robotics and Automation Letters*, vol. 6, no. 2, pp. 1864–1871, 2021.

[10] R. Steinmeyer, N.-S. P. Hyun, E. F. Helbling, and R. J. Wood, "Yaw torque authority for a flapping-wing micro-aerial vehicle," in *2019 International Conference on Robotics and Automation (ICRA)*, 2019, pp. 2481–2487.

[11] R. McGill, N.-S. P. Hyun, and R. J. Wood, "Modeling and control of flapping-wing micro-aerial vehicles with harmonic sinusoids," *IEEE Robotics and Automation Letters*, vol. 7, no. 2, pp. 746–753, 2021.

[12] Y. Chen, H. Zhao, J. Mao, P. Chirarattananon, E. F. Helbling, N.-S. P. Hyun, D. R. Clarke, and R. J. Wood, "Controlled flight of a microrobot powered by soft artificial muscles," *Nature*, vol. 575, no. 7782, pp. 324–329, 2019.

[13] Y. Chen, S. Xu, Z. Ren, and P. Chirarattananon, "Collision resilient insect-scale soft-actuated aerial robots with high agility," *IEEE Transactions on Robotics*, vol. 37, no. 5, pp. 1752–1764, 2021.

[14] Z. Ren, S. Kim, X. Ji, W. Zhu, F. Niroui, J. Kong, and Y. Chen, "A high-lift micro-aerial-robot powered by low-voltage and long-endurance dielectric elastomer actuators," *Advanced Materials*, p. 2106757, 2022.

[15] S. Kim, Y.-H. Hsiao, Y. Chen, J. Mao, and Y. Chen, "Firefly: An insect-scale aerial robot powered by electroluminescent soft artificial muscles," *IEEE Robotics and Automation Letters*, vol. 7, no. 3, pp. 6950–6957, 2022.

[16] X. Yang, Y. Chen, L. Chang, A. A. Calderón, and N. O. Pérez-Arancibia, "Bee+: A 95-mg four-winged insect-scale flying robot driven by twinned unimorph actuators," *IEEE Robotics and Automation Letters*, vol. 4, no. 4, pp. 4270–4277, 2019.

[17] F. M. Bos, D. Lentink, B. Van Oudheusden, and H. Bijl, "Influence of wing kinematics on aerodynamic performance in hovering insect flight," *Journal of fluid mechanics*, vol. 594, pp. 341–368, 2008.

[18] A. J. Bergou, S. Xu, and Z. J. Wang, "Passive wing pitch reversal in insect flight," *Journal of Fluid Mechanics*, vol. 591, pp. 321–337, 2007.

[19] Y. Chen, N. Gravish, A. L. Desbiens, R. Malka, and R. J. Wood, "Experimental and computational studies of the aerodynamic performance of a flapping and passively rotating insect wing," *Journal of Fluid Mechanics*, vol. 791, pp. 1–33, 2016.

[20] R. J. Wood, "The first takeoff of a biologically inspired at-scale robotic insect," *IEEE Transactions on Robotics*, vol. 24, no. 2, pp. 341–347, 2008.

[21] R. Malka, A. L. Desbiens, Y. Chen, and R. J. Wood, "Principles of microscale flexure hinge design for enhanced endurance. in 2014 ieee," in *RSJ International Conference on Intelligent Robots and Systems (IROS 2014)*, 2014, pp. 14–18.

[22] P. Chirarattananon, Y. Chen, E. F. Helbling, K. Y. Ma, R. Cheng, and R. J. Wood, "Dynamics and flight control of a flapping-wing robotic insect in the presence of wind gusts," *Interface focus*, vol. 7, no. 1, p. 20160080, 2017.

[23] S. B. Fuller, "Four wings: An insect-sized aerial robot with steering ability and payload capacity for autonomy," *IEEE Robotics and Automation Letters*, vol. 4, no. 2, pp. 570–577, 2019.

[24] Z. E. Teoh, "Design of hybrid passive and active mechanisms for control of insect-scale flapping-wing robots," Ph.D. dissertation, Harvard University, 2015.

[25] R. Ding, Y.-H. Hsiao, H. Jia, S. Bai, and P. Chirarattananon, "Passive wall tracking for a rotorcraft with tilted and ducted propellers using proximity effects," *IEEE Robotics and Automation Letters*, vol. 7, no. 2, pp. 1581–1588, 2022.